

3D Non-Stationary Wideband Tunnel Channel Models for 5G High-Speed Train Wireless Communications

Yu Liu^{ID}, Cheng-Xiang Wang^{ID}, *Fellow, IEEE*, Carlos F. Lopez^{ID}, George Goussetis^{ID}, *Senior Member, IEEE*, Yang Yang^{ID}, *Fellow, IEEE*, and George K. Karagiannidis^{ID}, *Fellow, IEEE*

Abstract—High-speed train (HST) communications in tunnels have attracted more and more research interests recently, especially within the framework of the fifth generation (5G) wireless networks. In this paper, based on cuboid-shape, three-dimensional (3D) non-stationary wideband geometry-based stochastic models (GBSMs) for HST tunnel scenarios are proposed. By considering the influence of the tunnel walls, a theoretical channel model is first established, which assumes clusters with an infinite number of scatterers randomly distributed on the tunnel walls. The corresponding simulation model is then developed and the method of equal areas is employed to obtain the discrete parameters, such as the azimuth and elevation angles. We derive and investigate the most important channel statistical properties of the proposed 3D GBSMs, including the time-variant autocorrelation function, spatial cross-correlation function, and Doppler power spectrum density. It is indicated that all statistical properties of the simulation model, verified by simulation results, can match very well with those of the theoretical model. Furthermore, a validation is presented by comparing the stationary regions of our proposed tunnel channel model to those of relevant measurement data.

Manuscript received August 25, 2017; revised March 21, 2018 and June 5, 2018; accepted December 14, 2018. Date of publication February 13, 2019; date of current version December 31, 2019. This work was supported in part by the EU H2020 ITN 5G Wireless Project under Grant 641985, in part by the EU H2020 RISE TESTBED Project under Grant 734325, in part by the EU FP7 QUICK Project under Grant PIRSESGA-2013-612652, in part by the EPSRC TOUCAN Project under Grant EP/L020009/1, in part by the Science and Technology Commission of Shanghai Municipality (STCSM) under Grant 18511106500, in part by the National Postdoctoral Program for Innovative Talents under Grant BX201700308, in part by the China Postdoctoral Science Foundation Funded Project under Grant 2017M622203 and in part by the Taishan Scholar Program of Shandong Province. The Associate Editor for this paper was C. F. Mecklenbräuer. (*Corresponding author: Cheng-Xiang Wang.*)

Y. Liu is with the Shandong Provincial Key Lab of Wireless Communication Technologies, School of Information Science and Engineering, Shandong University, Qingdao 266237, China (e-mail: xinwenliuyu@163.com).

C.-X. Wang is with the National Mobile Communications Research Laboratory, School of Information Science and Engineering, Southeast University, Nanjing 210096, China, and also with the School of Engineering and Physical Sciences, Institute of Sensors, Signals and Systems, Heriot-Watt University, Edinburgh EH14 4AS, U.K. (e-mail: chxwang@seu.edu.cn).

C. F. Lopez and G. Goussetis are with the School of Engineering and Physical Sciences, Institute of Sensors, Signals and Systems, Heriot-Watt University, Edinburgh EH14 4AS, U.K. (e-mail: cfl3@hw.ac.uk; g.goussetis@hw.ac.uk).

Y. Yang is with the Shanghai Institute of Fog Computing Technology, SIST, ShanghaiTech University, Shanghai 201210, China (e-mail: yangyang@shanghaitech.edu.cn).

G. K. Karagiannidis is with the Department of Electrical and Computer Engineering, Aristotle University of Thessaloniki, 54124 Thessaloniki, Greece (e-mail: geokarag@auth.gr).

Digital Object Identifier 10.1109/TITS.2019.2890992

Index Terms—Non-stationary GBSM, HST tunnel channels, statistical properties, time-variant parameters, measurement data.

I. INTRODUCTION

IN RECENT years, intelligent transportation systems (ITSs) have supported the increasing demand and rapid development of high-speed trains (HSTs) by incorporating novel communication technologies [1], [2], with the fifth generation (5G) wireless networks. As the communication demands of HST users continue to increase, large amounts of data need to be transmitted through wireless channels, which is far beyond the capacity of current HST communication systems [3]. In order to design and test the new generation HST communication systems, and develop future ITSs, accurate and efficient models which capture the key characteristics of HST channels are essential [4], [5].

There are more than twelve wireless channel scenarios that HSTs may encounter in practice, such as open space, cutting, viaduct, hilly terrain, tunnel, and station [6]. Because of the long limited visible space, bounding of tunnels, and roughness of interior walls, propagation characteristics of signals in tunnels are much different from those in other HST scenarios. Due to the confined space and high mobility of trains, radio waves inside tunnels can experience reflections on tunnel walls, diffractions by tunnel wedges, and scattering inside tunnel, which result in a more severe fast fading. All these phenomena induce waveguide effects, which influence the signal propagation [6] and make existing HST channel models [7] no longer suitable for tunnels.

In the open literature, the existing tunnel channel models can be classified into deterministic models, such as waveguide [8] and geometrical optical (GO) models [9]–[12], and stochastic models, such as geometry-based stochastic models (GBSMs) and finite-state markov models (FSMMs) [13], [14]. In [8], a model was proposed which adopted the modal theory to investigate the radio propagation. When signals propagate inside a tunnel, the propagation space can be divided into a *near region* and a *far region*. In the near region, there exists multiple propagation modes, while in the far region, the lowest order mode plays a dominant role. However, the waveguide model can only be applied to describe the far region and

thus it is not suitable for approximating signal propagation in the near region. Therefore, it would be more accurate to model HST tunnel channels by combining a waveguide model with another model. In [11], a GO model was proposed, where the electromagnetic (EM) field can be obtained by the summation of optical rays reflecting upon tunnel walls and diffracting on tunnel wedges. Moreover, the path loss and signal propagation delay at any location can be predicted. A multi-mode model for tunnel scenarios that combined the GO and the waveguide model using Poisson sum formulas, was proposed in [12], where the authors studied the received power at any position inside a tunnel. Based on real measurements, a FSMM for tunnel channels was proposed in [13] that took the train locations into consideration. Furthermore, the tunnel was divided into intervals in terms of distance, and in each distance interval, the FSMM was applied.

Most of aforementioned studies are focused on large-scale fading [15]–[18] but few on small-scale fading characteristics [19]. Specifically, based on the model presented in [12], a time-dependent multi-mode model for HST tunnels was presented in [20] and some small-scale fading characteristics were preliminarily investigated. Moreover, GBSMs for tunnel scenarios were studied in [21]. Unlike the models mentioned above, the ones presented in [21] can be used to describe scattering environments by geometry-based shapes. GBSMs can be further categorized as irregular-shaped GBSMs (IS-GBSMs) and regular-shaped GBSMs (RS-GBSMs) [22], depending on whether the effective scatterers are located on a regular shape or not. In [23], a 3D RS-GBSM for road tunnels in vehicle-to-vehicle (V2V) communications was proposed, and statistical properties, such as the spatial cross-correlation function (CCF) and temporal autocorrelation function (ACF), were investigated. However, the tunnel channel model in [23] is a wide-sense stationary (WSS) one, which ignores the non-stationarity resulting from fast movements of the transmitter (Tx), scatterers, and/or receiver (Rx). In [7], a non-stationary ellipse model was proposed to describe rural macrocell scenario for HST. The effective scatterers between the Tx and Rx are assumed to be randomly distributed on an ellipse with single-bounced (SB) components. Considering the characteristics of HST tunnel environments, more reflections are likely to occur inside tunnel. As presented in [24], the LoS and SB scattering components carry around 80% of the received power in tunnel scenarios. Hence, the line-of-sight (LoS), SB, and multi-bounced (MB) components all need to be considered in this paper. The model proposed in [7] cannot capture the key properties of the propagation inside tunnel. Moreover, the ellipse model proposed in [7] is two-dimensional (2D) and considers the azimuth angles only. Instead, a three-dimensional (3D) model considering both the azimuth and elevation angles is necessary that can better describe the propagation inside tunnels more accurately. Finally, a 3D non-stationary circular tunnel channel model was developed in [25], and the corresponding statistical properties were studied. Since different tunnel shapes will have different influences on channel characteristics, the channel model proposed in [25] can only describe the propagations

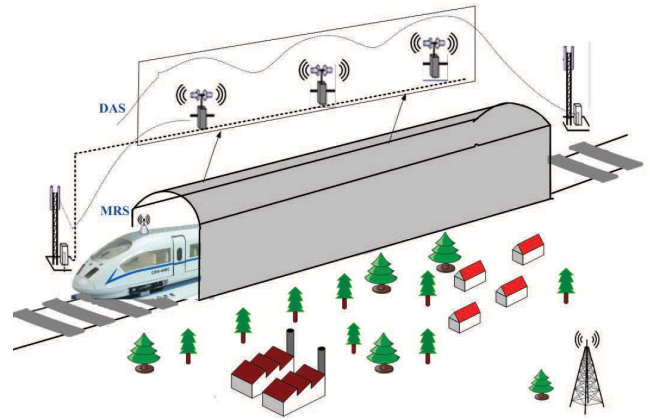


Fig. 1. A cellular architecture with DAS and MRS for HST tunnel MIMO communication systems.

in circular-like tunnels and is not suitable for other kinds of tunnels.

To the best of the authors' knowledge, non-stationary GBSMs considering time-variant small-scale fading statistical properties for HST rectangular-like tunnel scenarios, such as rectangular and horseshoe tunnels, are still missing from the literature. In this paper, we aim to develop a 3D non-stationary cuboid-based RS-GBSM for HST tunnel scenarios and investigate some of its time-variant statistical properties. The major contributions and novelties of this work can be summarized as follows.

- 1) A novel 3D non-stationary wideband theoretical GBSM for multiple-input multiple-output (MIMO) HST tunnel communication systems is proposed for the first time by considering the distributed antenna system (DAS) and mobile relay station (MRS). It involves time-variant angular parameters and time-variant distances between the Tx and Rx. Then, some important time-variant statistical properties, i.e., temporal ACF, spatial CCF, and Doppler power spectrum density (PSD), are derived and analyzed.
- 2) The corresponding sum-of-cisoids (SoC) simulation model is then developed, which considers a finite number of scatterers randomly distributed between the Tx and Rx. The positions of the scatterers are determined by the angular information, such as angles of arrival (AoAs) and angles of departure (AoDs), which are calculated using the method of equal area (MEA). We demonstrate the good agreement between the statistical properties of the simulation model, simulation results and theoretical model. The measurement data is also used for the validation of proposed GBSMs.

The remainder of this paper is organized as follows. The HST network architecture for tunnel scenarios and the distribution of scatterers inside a tunnel are described in Section II. In Section III, a 3D non-stationary wideband theoretical GBSM is proposed, and the corresponding SoC simulation model is given in Section IV. Results and analysis are provided in Section V, whereas conclusions are drawn in Section VI.

II. A HST NETWORK ARCHITECTURE FOR TUNNEL SCENARIOS

In this section, a brief description of a HST network architecture for tunnel scenarios is provided. Fig. 1 illustrates a typical tunnel scenario that incorporates a MIMO-based DAS system [26]–[28] and MRS as the underlying network architecture. All these technologies can be adopted to increase communication capacity and improve system performance inside tunnels. DAS using the radio over fiber (RoF) technology is utilized to overcome the limited visibility problem and provide better coverage inside the tunnel [29]. By implementing DAS, the propagation space can be divided into segments through repeaters connecting to the base station. We just focus on each segment to do the channel modeling. Moreover, the MRS is adopted as a regular base station and deployed on the surface of a train to improve the quality of received signals, address the spotty coverage problem, and mitigate high penetration losses of signals traveling into the train carriages [7]. Meanwhile, a MIMO technology is applied with P transmit and Q receive omnidirectional antenna elements to obtain higher capacity inside the tunnels.

Here, we assume that the train moves towards the fixed Tx. To depict the HST tunnel environments concisely, the rectangular-like tunnel channel can be abstracted as a cuboid-shape. When the train travels inside tunnel, the received signals are influenced by the tunnel ceiling, ground, and left/right walls. By considering the influences of elevation and azimuth angles, 3D non-stationary wideband tunnel channel models which can better mimic the propagation environment are proposed. In order to illustrate the above, a geometry-based clusters' distribution model is provided in Fig. 2, where we use the Cartesian coordinate system to describe the positions of the Tx and Rx. It should be mentioned here that the clusters concept is used to describe the scatterers, i.e., there are some clusters on the internal surfaces of the tunnel with some scatterers inside each cluster.

In Fig. 2, some clusters are assumed to be distributed randomly on the tunnel ceiling, ground and tunnel side walls, and the position of each cluster can be determined by the mean AoDs and AoAs in Tx and Rx side respectively, which are initially assumed to follow a Gaussian distribution [30]. Then, all the related parameters, such as distances between Tx and clusters, distances between clusters and Rx, can be obtained using the positions of clusters. The Tx is located near the tunnel side wall, while the Rx is placed at the middle of tunnel. The Tx and mobile Rx are equipped with a uniform linear antenna arrays consisting of P and Q antenna elements, and the inter-element spacings between the elements are denoted by Δx_T at the Tx and Δx_R at the Rx. In Fig. 2, only one SB and MB components are depicted for clarity. The mean azimuth AoD (AAoD), elevation AoD (EAoD), azimuth AoA (AAoA), and elevation AoA (EAoA) are denoted by $\alpha_{ST}^l(t)$, $\beta_{ST}^l(t)$, $\alpha_{SR}^i(t)$, and $\beta_{SR}^i(t)$ respectively in the SB case, and denoted by $\alpha_{MT}^i(t)$, $\beta_{MT}^i(t)$, $\alpha_{MR}^i(t)$, and $\beta_{MR}^i(t)$ respectively in the MB case. It should be mentioned that the AoAs and AoDs are dependent for the SB case, but independent for the MB case.

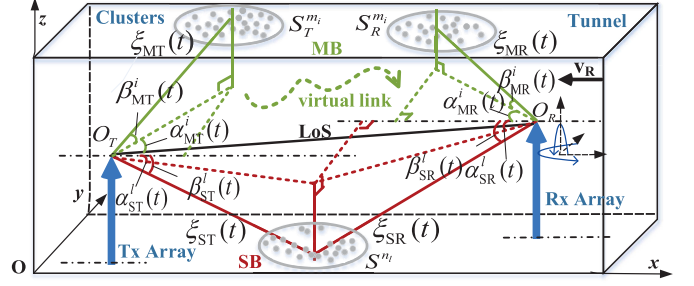


Fig. 2. A 3D cuboid-shape GBSM for tunnel scenarios.

III. A 3D NON-STATIONARY WIDEBAND THEORETICAL GBSM

A. Description of the Non-Stationary Wideband MIMO Theoretical Channel Model

Based on the previously presented network architecture, in this section, a 3D wideband theoretical GBSM is proposed and time-variant statistical properties are derived. Combining the WINNER II model [30], [31] and the confined tunnel space, the HST tunnel propagation environment can be characterized as a 3D cuboid model as shown in Fig. 2. The corresponding parameters in Fig. 2 are defined in Table I. The channel impulse response (CIR) consists of the LoS and NLoS components. The NLoS components contain the SB and MB components reflected by tunnel ceiling, ground, and two side walls. It is assumed that there are totally L clusters with SB components and I clusters with MB components randomly distributed on the tunnel internal surfaces. The complex CIR between the p th element of the Tx and the q th element of the Rx can be expressed as [7]

$$h_{pq}(t, \tau) = h_{pq}^{\text{LoS}}(t) \cdot \delta(\tau - \tau^{\text{LoS}}(t)) + \sum_{l=1}^L h_{pq,l}^{\text{SB}}(t) \times \delta(\tau - \tau_l^{\text{SB}}(t)) + \sum_{i=1}^I h_{pq,i}^{\text{MB}}(t) \cdot \delta(\tau - \tau_i^{\text{MB}}(t)) \quad (1)$$

where $\tau^{\text{LoS}}(t)$ denotes the propagation time delay of the LoS component, $\tau_l^{\text{SB}}(t)$ denotes the mean propagation time delay of the l th cluster, and $\tau_i^{\text{MB}}(t)$ denotes the mean propagation time delay of the i th twin-cluster.

In (1), the LoS component can be expressed as

$$h_{pq}^{\text{LoS}}(t) = \sqrt{\frac{K_{pq}}{K_{pq} + 1}} e^{-\frac{j2\pi \epsilon_{pq}(t)}{\lambda}} \times e^{j2\pi f_{R_{\max}} t \cos(\alpha_R^{\text{LoS}}(t) - \gamma_R) \cos \beta_R^{\text{LoS}}(t)} \quad (2)$$

and the SB components can be expressed as

$$h_{pq,l}^{\text{SB}}(t) = \sqrt{\frac{P_l}{K_{pq} + 1}} \lim_{N_l \rightarrow \infty} \sum_{n_l=1}^{N_l} \sqrt{\frac{1}{N_l}} e^{j(\varphi_{n_l} - \frac{2\pi \epsilon_{pq,n_l}(t)}{\lambda})} \times e^{j2\pi f_{R_{\max}} t \cos(\alpha_{SR}^{n_l}(t) - \gamma_R) \cos \beta_{SR}^{n_l}(t)} \quad (3)$$

where

$$\varepsilon_{pq,n_l}(t) = \varepsilon_{p,n_l}(t) + \varepsilon_{q,n_l}(t) \quad (4)$$

Here, $\varepsilon_{p,n_l}(t)$ is the distance between the T_p and the n_l th scatterer of the l th cluster, and $\varepsilon_{q,n_l}(t)$ is the distance between the n_l th scatterer of the l th cluster and the T_q in the SB case. Based on the geometrical relationship in Fig. 3(a) and the applications of the law of cosines, we have [7]

$$\varepsilon_{p,n_l}(t) \approx \zeta_{ST}(t) - \frac{P-2p+1}{2} \Delta x_T \cos \alpha_{ST}^{n_l}(t) \cos \beta_{ST}^{n_l}(t) \quad (5)$$

$$\varepsilon_{q,n_l}(t) \approx \zeta_{SR}(t) - \frac{Q-2q+1}{2} \Delta x_R \cos \alpha_{SR}^{n_l}(t) \cos \beta_{SR}^{n_l}(t) \quad (6)$$

$$\zeta_{ST}(t) = \sqrt{(x_T - x_{SR}^{n_l})^2 + (y_T - y_{SR}^{n_l})^2 + (z_T - z_{SR}^{n_l})^2} \quad (7)$$

$$\zeta_{SR}(t) = \sqrt{(x_R - x_{SR}^{n_l})^2 + (y_R - y_{SR}^{n_l})^2 + (z_R - z_{SR}^{n_l})^2}. \quad (8)$$

More detailed calculations of (5) and (6) are provided in Appendix A. The position coordinates $(x_{SR}^{n_l}, y_{SR}^{n_l}, z_{SR}^{n_l})$ of the n_l th scatterer of l th SB cluster can be computed as

$$\begin{cases} x_{SR}^{n_l} = x_R - vt - G_R(t) \cos \beta_{SR}^{n_l}(t) \cos \alpha_{SR}^{n_l}(t) \\ y_{SR}^{n_l} = y_R + G_R(t) \cos \beta_{SR}^{n_l}(t) \sin \alpha_{SR}^{n_l}(t) \\ z_{SR}^{n_l} = z_R + G_R(t) \sin \beta_{SR}^{n_l}(t). \end{cases} \quad (9)$$

For the ceiling and bottom of the tunnel, $G_R(t) = \frac{z-z_R}{\sin \beta_{SR}^{n_l}(t)}$, hinges on $z = z_t$ of ceiling and $z = z_b$ of bottom. For the left and right walls, $G_R(t) = \frac{y-y_R}{\cos \beta_{SR}^{n_l}(t) \sin \alpha_{SR}^{n_l}(t)}$ depends on $y = y_{lw}$ of the left wall and $y = y_{rw}$ of the right wall. Furthermore, the AoDs and AoAs are correlated with each other. The AoDs for the SB components can be expressed as

$$\sin \alpha_{ST}^{n_l}(t) = \frac{y_{SR}^{n_l} - y_T}{\sqrt{(x_{SR}^{n_l} - x_T)^2 + (z_{SR}^{n_l} - z_T)^2}} \quad (10)$$

$$\sin \beta_{ST}^{n_l}(t) = \frac{z_{SR}^{n_l} - z_T}{\sqrt{(x_{SR}^{n_l} - x_T)^2 + (y_{SR}^{n_l} - y_T)^2 + (z_{SR}^{n_l} - z_T)^2}}. \quad (11)$$

The position coordinates $(x_{SR}^{n_l}, y_{SR}^{n_l}, z_{SR}^{n_l})$ including AoAs in (10) and (11) can be achieved from (9). $\alpha_{ST}^{n_l}(t)$ and $\alpha_{SR}^{n_l}(t)$ denote the azimuth angles of the Tx and Rx of the SB components respectively, and $\beta_{ST}^{n_l}(t)$ and $\beta_{SR}^{n_l}(t)$ denote the elevation angles of the Tx and Rx, respectively. The positions of the Tx and Rx are (x_T, y_T, z_T) and (x_R, y_R, z_R) , respectively, and the positions of clusters can be obtained by the mean AAoAs $\alpha_{SR}^l(t)$ and mean EAoAs $\beta_{SR}^l(t)$ at the Rx. Once the mean angles are determined, the positions of clusters are fixed, then all the information of tunnel channel, including the distances, the AoAs, the AoDs, and the delays, can be acquired.

Moreover, the MB components of the tunnel walls can be expressed as

$$\begin{aligned} h_{pq,i}^{MB}(t) &= \sqrt{\frac{P_i}{K_{pq} + 1}} \lim_{M_i \rightarrow \infty} \sum_{m_{i,1}=1}^{M_{i,1}} \sum_{m_{i,2}=1}^{M_{i,2}} \sqrt{\frac{1}{M_{i,1} M_{i,2}}} \\ &\times e^{j(\varphi_{m_i} - \frac{2\pi \cdot \varepsilon_{pq,m_{i,1}m_{i,2}}(t)}{\lambda})} \\ &\times e^{j2\pi f_R \max\{t \cos(\alpha_{MR}^{m_{i,2}}(t) - \gamma_R) \cos \beta_{MR}^{m_{i,2}}(t)\}} \end{aligned} \quad (12)$$

where

$$\begin{aligned} \varepsilon_{pq,m_{i,1}m_{i,2}}(t) &= \varepsilon_{p,m_{i,1}m_{i,2}}(t) + \varepsilon_{q,m_{i,2}m_{i,2}}(t) + \tau_{m_{i,1}m_{i,2}} \cdot c \end{aligned} \quad (13)$$

$$\varepsilon_{p,m_{i,1}m_{i,1}}(t) \approx \zeta_{MT}(t) - \frac{P-2p+1}{2} \Delta x_T \cos \alpha_{MT}^{m_{i,1}}(t) \cos \beta_{MT}^{m_{i,1}}(t) \quad (14)$$

$$\varepsilon_{q,m_{i,2}m_{i,2}}(t) \approx \zeta_{MR}(t) - \frac{Q-2q+1}{2} \Delta x_R \cos \alpha_{MR}^{m_{i,2}}(t) \cos \beta_{MR}^{m_{i,2}}(t) \quad (15)$$

$$\zeta_{MT}(t) = \sqrt{(x_T - x_{MT}^{m_{i,1}})^2 + (y_T - y_{MT}^{m_{i,1}})^2 + (z_T - z_{MT}^{m_{i,1}})^2} \quad (16)$$

$$\zeta_{MR}(t) = \sqrt{(x_R - x_{MR}^{m_{i,2}})^2 + (y_R - y_{MR}^{m_{i,2}})^2 + (z_R - z_{MR}^{m_{i,2}})^2}. \quad (17)$$

Here, $\alpha_{MT}^{m_{i,1}}(t)$ and $\alpha_{MR}^{m_{i,2}}(t)$ denote the azimuth angles of the Tx and Rx of MB components, respectively. $\beta_{MT}^{m_{i,1}}(t)$ and $\beta_{MR}^{m_{i,2}}(t)$ denote the elevation angles of the Tx and Rx of the MB components, respectively. For the MB case, it mainly consists of twin clusters, one is a representation at Tx side modeling first bounce, and another one is a representation at the Rx side modeling the last bounce. The propagation space between these two clusters can be abstracted as a virtual link [32], denoted by $\tau_{m_{i,1}m_{i,2}}$, and follows exponential distribution. The positions of these two representations are determined by $(x_{MT}^{m_{i,1}}, y_{MT}^{m_{i,1}}, z_{MT}^{m_{i,1}})$ and $(x_{MR}^{m_{i,2}}, y_{MR}^{m_{i,2}}, z_{MR}^{m_{i,2}})$, respectively. The relations between the coordinates and angles can be expressed as follows

$$\begin{cases} x_{MT}^{m_{i,1}} = G_T(t) \cos \beta_{MT}^{m_{i,1}}(t) \cos \alpha_{MT}^{m_{i,1}}(t) \\ y_{MT}^{m_{i,1}} = G_T(t) \cos \beta_{MT}^{m_{i,1}}(t) \sin \alpha_{MT}^{m_{i,1}}(t) \\ z_{MT}^{m_{i,1}} = G_T(t) \sin \beta_{MT}^{m_{i,1}}(t). \end{cases} \quad (18)$$

Similar to $G_R(t)$ in the SB components, the intermediate variable $G_T(t) = \frac{z-z_T}{\sin \beta_{MT}^{m_{i,1}}(t)}$ depends on variable $z = z_t$ and $z = z_b$ for the ceiling and ground respectively, and $G_T(t) = \frac{y-y_T}{\cos \beta_{MT}^{m_{i,1}}(t) \sin \alpha_{MT}^{m_{i,1}}(t)}$ depends on variable $y = y_{lw}$ and $y = y_{rw}$ for left and right walls.

It is worth mentioning that, in (2), (3), (4), and (13), parameters $\alpha_{MT}^{m_{i,1}}(t)$, $\beta_{MT}^{m_{i,1}}(t)$, $\alpha_{MR}^{m_{i,2}}(t)$, $\beta_{MR}^{m_{i,2}}(t)$, and $\varepsilon_{pq,m_{i,1}m_{i,2}}(t)$ ($m = 1, \dots, M$) are time-variant, which reflect the non-stationarity of channel. Once the parameters are not time-varying, our model can be reduced to a WSS one. The symbol K_{pq} designates the Ricean K factor, and c represents the speed of light. The phases φ_{m_i} ($i = 1, \dots, I$) are independent and identically distributed random variables with uniform distribution over $[-\pi, \pi)$. The maximum

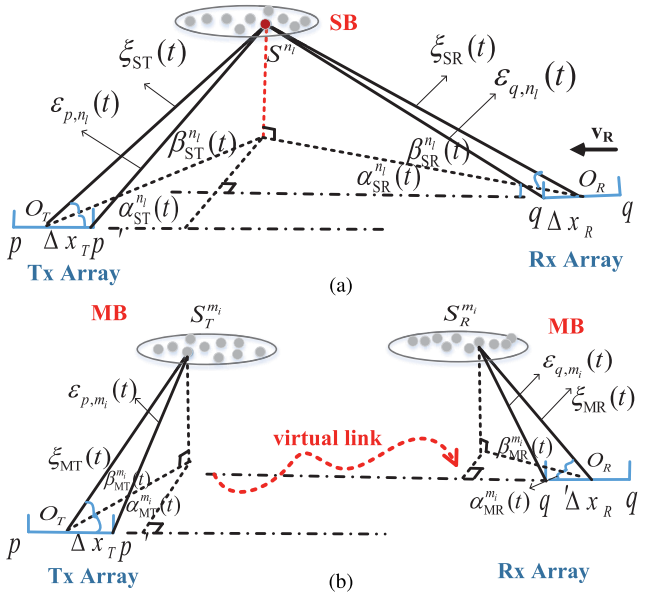


Fig. 3. Geometrical relationship of the SB and MB cases: (a) Time-varying angular parameters of the SB components of the HST tunnel channel model. (b) Time-varying angular parameters of the MB components of the HST tunnel channel model.

Doppler frequency shift is denoted by $f_{R \max} = \frac{v_R f_c}{c}$, which is determined by the carrier frequency f_c , the speed of the train v_R and the speed of light c . Note that the AAoD $\alpha_{MT}^{m_{i,1}}(t)$, EAoD $\beta_{MT}^{m_{i,1}}(t)$, and the AAoA $\alpha_{MR}^{m_{i,2}}(t)$, EAoA $\beta_{MR}^{m_{i,2}}(t)$ of the MB components are assumed mutually independent. The geometrical relationships among the AAoD, EAoD, AAoA, EAoA can be given in Fig. 3 (a) in the SB case and in Fig. 3 (b) in the MB case. The related parameters are defined in Table I.

For the proposed 3D theoretical channel model, the number of scatterers is considered as approaching infinite. Therefore, the discrete AAoD, EAoD, AAoA, and EAoA can be replaced by continuous random variables. Here, the distributions of azimuth and elevation angles at the Tx and Rx are assumed to follow 2D von Mises distributions [32], and both of which are mutually independent. Therefore, the PDF of arrivals of the corresponding cluster can be expressed as

$$f(\alpha_{MR}^{m_{i,2}}, \beta_{MR}^{m_{i,2}}) \triangleq \frac{e^{[u_1 \cos(\alpha_{MR}^{m_{i,2}} - \alpha_{MR}^i) + u_2 \cos(\beta_{MR}^{m_{i,2}} - \beta_{MR}^i)]}}{[2\pi I_0(k_1)][2\pi I_0(k_2)]} \quad (19)$$

where $\alpha_{MR}^i(t)$, $\beta_{MR}^i(t)$ account for the mean values of azimuth angles $\alpha_{MR}^{m_{i,2}}(t)$ and elevation angles $\beta_{MR}^{m_{i,2}}(t)$, respectively. $I_0(\cdot)$ is the zero-th order modified Bessel function of the first kind. Furthermore, k_1, k_2 ($k_1, k_2 \geq 0$) are real-valued parameters of clusters, which can control the width of the distribution relative to the mean direction identified by $\alpha_{MR}^i(t)$ and $\beta_{MR}^i(t)$. Note that the von Mises distribution has been widely used to model angular dispersions [32], and is a general function including some well-known PDFs as special cases, e.g., uniform PDF. Moreover, based on the geometric relations in Fig. 3 (b), the time-varying function of mean AAoA $\alpha_{MR}^i(t)$ and mean EAoA $\beta_{MR}^i(t)$ in the MB case can be derived as (20) and (21), shown at the bottom of the next page, respectively. Meanwhile,

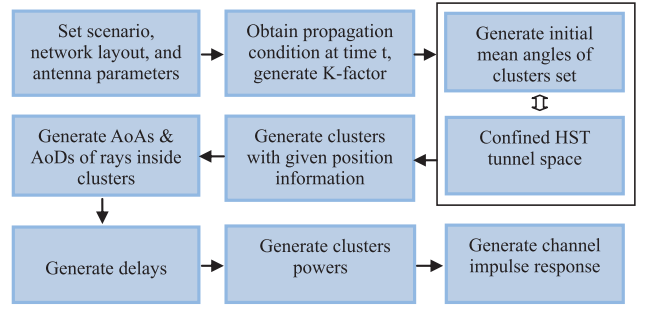


Fig. 4. Flowchart of the generation of the HST tunnel CIR.

the mean AAoA $\alpha_{SR}^l(t)$ and mean EAoA $\beta_{SR}^l(t)$ in the SB case can be acquired analogously to those in the MB case.

B. Power of Different Clusters

The power of clusters in the tunnel follows exponential profile, using WINNER II channel model as a reference [30]. Therefore, random power of the l th one-cluster or the i th twin-cluster can be expressed as [30]. Here, the power associated the SB cluster can be expressed as

$$P_l = e^{\frac{(\chi-1)(-\tau_l)}{\chi\sigma_\tau}} \times 10^{\frac{-Z_l}{10}}, \quad (l = 1, \dots, L) \quad (22)$$

where χ denotes the delay scaling parameter, σ_τ denotes the delay spread, and Z_l is the per cluster shadowing term in dB. The calculated power is normalized to make the total received power equal to 1.

Finally, the generation procedure of the CIR is presented in Fig. 4, which consists of the generation of mean angles of clusters in tunnel space and the calculation of parameters, such as delays, powers, AoAs and AoDs.

C. Statistical Properties of the Theoretical Model

In this section, we will derive some typical statistical properties of the proposed non-stationary theoretical HST tunnel channel model.

1) *ST CF*: The correlation properties of two arbitrary channel impulse responses of $h_{pq}(t, \tau)$ and $h_{p'q'}^*(t - \Delta t, \tau)$ of the wideband tunnel channel model can be defined as the summation of all the clusters with no inter-correlation, i.e., assuming uncorrelated scattering in the delay domain. The correlation function of each cluster can be expressed as follows

$$R_h(t, \Delta x_T, \Delta x_R, \Delta t) = E \left[h_{pq}(t) h_{p'q'}^*(t - \Delta t) \right] \quad (23)$$

where $(\cdot)^*$ denotes the complex conjugate operation, and $E[\cdot]$ denotes the expectation operator. Assuming that the LoS, SB, and MB components are independent of each other, and using (2), (3), (4), and (13), the ST CF can be also expressed as

$$R_h(t, \Delta x_T, \Delta x_R, \Delta t) = R_h^{\text{LoS}}(t, \Delta x_T, \Delta x_R, \Delta t) + R_h^{\text{SB}}(t, \Delta x_T, \Delta x_R, \Delta t) + R_h^{\text{MB}}(t, \Delta x_T, \Delta x_R, \Delta t). \quad (24)$$

TABLE I
DEFINITION OF PARAMETERS

Parameters	Definition
$\alpha_{ST}^l(t), \beta_{ST}^l(t)$	the mean AAoD and EAoD in SB case
$\alpha_{SR}^l(t), \beta_{SR}^l(t)$	the mean AAoA and EAoA in SB case
$\alpha_{MT}^i(t), \beta_{MT}^i(t)$	the mean AAoD and EAoD in MB case
$\alpha_{MR}^i(t), \beta_{MR}^i(t)$	the mean AAoA and EAoA in MB case
$\alpha_{ST}^{n_l}(t), \beta_{ST}^{n_l}(t)$	the AAoD and EAoD of the n_l th ray of the l th cluster in SB case
$\alpha_{SR}^{n_l}(t), \beta_{SR}^{n_l}(t)$	the AAoA and EAoA of the n_l th ray of the l th cluster in SB case
$\alpha_{MT}^{m_{i,1}}(t), \beta_{MT}^{m_{i,1}}(t)$	the AAoD and EAoD of the $m_{i,1}$ th ray of the i th cluster in MB case
$\alpha_{MR}^{m_{i,1}}(t), \beta_{MR}^{m_{i,1}}(t)$	the AAoA and EAoA of the $m_{i,1}$ th ray of the i th cluster in MB case
$\alpha_{MT}^{m_{i,2}}(t), \beta_{MT}^{m_{i,2}}(t)$	the AAoD and EAoD of the $m_{i,2}$ th ray of the i th cluster in MB case
$\alpha_{MR}^{m_{i,2}}(t), \beta_{MR}^{m_{i,2}}(t)$	the AAoA and EAoA of the $m_{i,2}$ th ray of the i th cluster in MB case
z_t, z_b	the z coordinates of tunnel ceiling and tunnel ground
y_{lw}, y_{rw}	the y coordinates of tunnel left wall and tunnel right wall
$\Delta x_T, \Delta x_R$	antenna elements spacings of Tx and Rx
$\varepsilon_{pq}(t)$	the distance $d(T_p, T_q)$ in LoS case
$\varepsilon_{pq, n_l}(t)$	the total distance between T_p and T_q in SB case
$\varepsilon_{p, n_l}(t), \varepsilon_{q, n_l}(t)$	the distance $d(S^{n_l}, T_p)$, the distance $d(S^{n_l}, T_q)$ in SB case
$\xi_{ST}(t), \xi_{SR}(t)$	the distance $d(O_T, S^{n_l})$, the distance $d(S^{n_l}, O_R)$
$\varepsilon_{pq, m_{i,1} m_{i,2}}(t)$	the total distance between T_p and T_q in MB case
$\varepsilon_{p, m_{i,1} m_{i,2}}(t), \varepsilon_{q, m_{i,2} m_{i,2}}(t)$	the distance $d(T_p, S_T^{m_{i,1}})$, the distance $d(S_R^{m_{i,2}}, T_q)$ in MB case
$\xi_{MT}(t), \xi_{MR}(t)$	the distance $d(O_T, S_T^{m_{i,1}})$, the distance $d(S_R^{m_{i,2}}, O_R)$

–In the case of the LoS component,

$$R_h^{\text{LoS}}(t, \Delta x_T, \Delta x_R, \Delta t) = \frac{K_{pq}}{K_{pq} + 1} e^{j2\pi \frac{\varepsilon_{p'q'}(t-\Delta t) - \varepsilon_{pq}(t)}{\lambda}} \times e^{j2\pi f_{R\max} \Delta t \cos(\alpha_R^{\text{LoS}}(t) - \gamma_R) \cos \beta_R^{\text{LoS}}(t)} \quad (25)$$

where the time delay of LoS component can be obtained by the following geometrical relations

$$\varepsilon_{p'q'}(t - \Delta t) - \varepsilon_{pq}(t) = \sqrt{(x_q + q \Delta x_R - v(t - \Delta t) - x_p - p \Delta x_T)^2 + (y_p - y_q)^2} - \sqrt{(x_q - vt - x_p)^2 + (y_p - y_q)^2}. \quad (26)$$

–In the case of SB components,

$$R_h^{\text{SB}}(t, \Delta x_T, \Delta x_R, \Delta t) = \frac{P_l}{(K_{pq} + 1)N_l} \int_{-\pi}^{\pi} \int_{-\pi/2}^{\pi/2} e^{j2\pi \frac{(\varepsilon_{pq, n_l}(t) - \varepsilon_{p'q', n_l}(t - \Delta t))}{\lambda}} \times e^{j2\pi f_{R\max} \Delta t \cos(\alpha_{SR}^{n_l} - \gamma_R) \cos \beta_{SR}^{n_l}} f(\alpha_{SR}^{n_l}, \beta_{SR}^{n_l}) d(\alpha_{SR}^{n_l}, \beta_{SR}^{n_l}) \quad (27)$$

where the propagation time between different antenna elements can be derived as

$$\varepsilon_{pq, n_l}(t) - \varepsilon_{p'q', n_l}(t - \Delta t) = \varepsilon_{p, n_l}(t) + \varepsilon_{q, n_l}(t) - \varepsilon_{p', n_l}(t - \Delta t) - \varepsilon_{q', n_l}(t - \Delta t). \quad (28)$$

–In the case of MB components,

$$R_h^{\text{MB}}(t, \Delta x_T, \Delta x_R, \Delta t) = \frac{P_i}{(K_{pq} + 1)M_{i,1}M_{i,2}} \times \int_{-\pi}^{\pi} \int_{-\pi}^{\pi} \int_{-\pi/2}^{\pi/2} \int_{-\pi/2}^{\pi/2} e^{j2\pi \frac{(\varepsilon_{pq, m_{i,1} m_{i,2}}(t) - \varepsilon_{p'q', m_{i,1} m_{i,2}}(t - \Delta t))}{\lambda}} \times e^{j2\pi f_{R\max} \Delta t \cos(\alpha_{MR}^{m_{i,2}} - \gamma_R) \cos \beta_{MR}^{m_{i,2}}} f(\alpha_{MR}^{m_{i,2}}, \beta_{MR}^{m_{i,2}}) \times f(\alpha_{MT}^{m_{i,1}}, \beta_{MT}^{m_{i,1}}) d(\alpha_{MR}^{m_{i,2}}, \beta_{MR}^{m_{i,2}}) d(\alpha_{MT}^{m_{i,1}}, \beta_{MT}^{m_{i,1}}). \quad (29)$$

2) *Time-Variant Spatial CCF*: According to the above expressions, the time-variant spatial CCF between arbitrary channel coefficients can be obtained by imposing $\Delta t = 0$ in (24). Based on (24), the specific time-variant spatial CCF can be expressed as

$$\rho_h(t, \Delta x_T, \Delta x_R) = R_h(t, \Delta x_T, \Delta x_R, 0) = \rho_h^{\text{LoS}}(t, \Delta x_T, \Delta x_R) + \rho_h^{\text{SB}}(t, \Delta x_T, \Delta x_R) + \rho_h^{\text{MB}}(t, \Delta x_T, \Delta x_R). \quad (30)$$

–In the case of LoS component,

$$\rho_h^{\text{LoS}}(t, \Delta x_T, \Delta x_R) = R_h^{\text{LoS}}(t, \Delta x_T, \Delta x_R, 0) = E \left[h_{pq}^{\text{LoS}}(t) h_{p'q'}^{\text{LoS}*}(t) \right] = \frac{K_{pq}}{K_{pq} + 1} e^{j2\pi \frac{(\varepsilon_{p'q'}(t) - \varepsilon_{pq}(t))}{\lambda}}. \quad (31)$$

$$\alpha_{MR}^i(t) = \arccos \frac{\xi_{MR}(t_0) \cos \alpha_{MR}^i(t_0) \cos \beta_{MR}^i(t_0) - v_R t}{\sqrt{(\xi_{MR}(t_0) \cos \beta_{MR}^i(t_0))^2 + (v_R t)^2 - 2(\xi_{MR}(t_0) \cos \beta_{MR}^i(t_0)) v_R t \cos \alpha_{MR}^i(t_0)}} \quad (20)$$

$$\beta_{MR}^i(t) = \arccos \frac{\sqrt{(\xi_{MR}(t_0) \cos \beta_{MR}^i(t_0))^2 + (v_R t)^2 - 2\xi_{MR}(t_0) v_R t \cos \alpha_{MR}^i(t_0) \cos \beta_{MR}^i(t_0)}}{\sqrt{(\xi_{MR}(t_0))^2 + (v_R t)^2 - 2\xi_{MR}(t_0) v_R t \cos \alpha_{MR}^i(t_0) \cos \beta_{MR}^i(t_0)}}. \quad (21)$$

–In the case of SB components,

$$\begin{aligned}
\rho_h^{\text{SB}}(t, \Delta x_T, \Delta x_R) &= R_h^{\text{SB}}(t, \Delta x_T, \Delta x_R, 0) = E \left[h_{pq}^{\text{SB}}(t) h_{p'q'}^{\text{SB}*}(t) \right] \\
&= \frac{P_l}{(K_{pq} + 1)N_l} \int_{-\pi}^{\pi} \int_{-\pi/2}^{\pi/2} e^{j2\pi \frac{(\varepsilon_{pq,n_l}(t) - \varepsilon_{p'q',n_l}(t))}{\lambda}} \\
&\quad \times f(\alpha_{\text{SR}}^{n_l}, \beta_{\text{SR}}^{n_l}) d\alpha_{\text{SR}}^{n_l} d\beta_{\text{SR}}^{n_l} \\
&= \frac{P_l}{(K_{pq} + 1)N_l} \int_{-\pi}^{\pi} \int_{-\pi/2}^{\pi/2} e^{j2\pi \frac{((k_p - k_{p'})\Delta x_T \cos(\alpha_{\text{ST}}^{n_l}) \cos(\beta_{\text{ST}}^{n_l}))}{\lambda}} \\
&\quad \times e^{j2\pi \frac{(k_q - k_{q'})\Delta x_R \cos(\alpha_{\text{SR}}^{n_l}) \cos(\beta_{\text{SR}}^{n_l})}{\lambda}} f(\alpha_{\text{SR}}^{n_l}, \beta_{\text{SR}}^{n_l}) d\alpha_{\text{SR}}^{n_l} d\beta_{\text{SR}}^{n_l}. \tag{32}
\end{aligned}$$

–In the case of MB components,

$$\begin{aligned}
\rho_h^{\text{MB}}(t, \Delta x_T, \Delta x_R) &= R_h^{\text{MB}}(t, \Delta x_T, \Delta x_R, 0) \\
&= \frac{P_m}{(K_{pq} + 1)M_{i,1}M_{i,2}} \int_{-\pi}^{\pi} \int_{-\pi}^{\pi} \int_{-\pi/2}^{\pi/2} \int_{-\pi/2}^{\pi/2} \\
&\quad \times e^{j2\pi \frac{(\varepsilon_{pq,m_{i,1}m_{i,2}}(t) - \varepsilon_{p'q',m_{i,1}m_{i,2}}(t))}{\lambda}} \\
&\quad \times f(\alpha_{\text{MT}}^{m_{i,1}}, \beta_{\text{MT}}^{m_{i,1}}) f(\alpha_{\text{MR}}^{m_{i,2}}, \beta_{\text{MR}}^{m_{i,2}}) d(\alpha_{\text{MT}}^{m_{i,1}}, \beta_{\text{MT}}^{m_{i,1}}) \\
&\quad \times d(\alpha_{\text{MR}}^{m_{i,2}}, \beta_{\text{MR}}^{m_{i,2}}). \tag{33}
\end{aligned}$$

3) *Time-Variant ACF*: From (24), the time-variant ACF can be derived by imposing $\Delta x_R = 0$ and $\Delta x_T = 0$.

$$\begin{aligned}
r_h(t, \Delta t) &= R_h(t, 0, 0, \Delta t) \\
&= r_h^{\text{LoS}}(t, \Delta t) + r_h^{\text{SB}}(t, \Delta t) + r_h^{\text{MB}}(t, \Delta t) \tag{34}
\end{aligned}$$

–In the case of the LOS component,

$$\begin{aligned}
r_h^{\text{LoS}}(t, \Delta t) &= E \left[h_{pq}^{\text{LoS}}(t) h_{pq}^{\text{LoS}*}(t - \Delta t) \right] \\
&= \frac{K_{pq}}{(K_{pq} + 1)} e^{-j2\pi \frac{(\varepsilon_{pq}(t) - \varepsilon_{pq}(t - \Delta t))}{\lambda}} \\
&\quad \times e^{j2\pi f_{R\max} \Delta t \cos(\alpha_R^{\text{LoS}}(t - \Delta t) - \gamma_R) \cos \beta_R^{\text{LoS}}(t - \Delta t)}. \tag{35}
\end{aligned}$$

–In the case of SB components,

$$\begin{aligned}
r_h^{\text{SB}}(t, \Delta t) &= E \left[h_{pq}^{\text{SB}}(t) h_{pq}^{\text{SB}*}(t - \Delta t) \right] \\
&= \frac{P_l}{(K_{pq} + 1)N_l} \int_{-\pi}^{\pi} \int_{-\pi/2}^{\pi/2} e^{j2\pi \frac{(\varepsilon_{pq,n_l}(t) - \varepsilon_{pq,n_l}(t - \Delta t))}{\lambda}} \\
&\quad \times e^{j2\pi f_{R\max} \Delta t \cos(\alpha_{\text{SR}}^{n_l} - \gamma_R) \cos \beta_{\text{SR}}^{n_l}} f(\alpha_{\text{SR}}^{n_l}, \beta_{\text{SR}}^{n_l}) d\alpha_{\text{SR}}^{n_l} d\beta_{\text{SR}}^{n_l}. \tag{36}
\end{aligned}$$

–In the case of MB components,

$$\begin{aligned}
r_h^{\text{MB}}(t, \Delta t) &= E \left[h_{pq}^{\text{MB}}(t) h_{pq}^{\text{MB}*}(t - \Delta t) \right] \\
&= \frac{P_m}{(K_{pq} + 1)M_{i,1}M_{i,2}} \\
&\quad \times \int_{-\pi}^{\pi} \int_{-\pi}^{\pi} \int_{-\pi/2}^{\pi/2} \int_{-\pi/2}^{\pi/2} e^{j2\pi \frac{(\varepsilon_{pq,m_{i,1}m_{i,2}}(t) - \varepsilon_{pq,m_{i,1}m_{i,2}}(t - \Delta t))}{\lambda}} \\
&\quad \times e^{j2\pi f_{R\max} \Delta t \cos(\alpha_{\text{MR}}^{m_{i,2}} - \gamma_R) \cos \beta_{\text{MR}}^{m_{i,2}}} f(\alpha_{\text{MT}}^{m_{i,1}}, \beta_{\text{MT}}^{m_{i,1}}) \\
&\quad \times f(\alpha_{\text{MR}}^{m_{i,2}}, \beta_{\text{MR}}^{m_{i,2}}) d(\alpha_{\text{MT}}^{m_{i,1}}, \beta_{\text{MT}}^{m_{i,1}}) d(\alpha_{\text{MR}}^{m_{i,2}}, \beta_{\text{MR}}^{m_{i,2}}). \tag{37}
\end{aligned}$$

4) *Time-Variant Doppler PSD*: The PSD is also an important channel statistical property, which can reflect the distribution of power along the Doppler frequency. It can be derived by the Fourier transform of the temporal ACF with the respect to Δt .

$$S_h(f_D, t) = S_h^{\text{LoS}}(f_D, t) + S_h^{\text{SB}}(f_D, t) + S_h^{\text{MB}}(f_D, t) \tag{38}$$

–In the case of LoS component,

$$S_h^{\text{LoS}}(f_D, t) = \int_{-\infty}^{\infty} r_h^{\text{LoS}}(t, \Delta t) e^{-j2\pi f_D \Delta t} d\Delta t. \tag{39}$$

–In the case of SB components,

$$S_h^{\text{SB}}(f_D, t) = \int_{-\infty}^{\infty} r_h^{\text{SB}}(t, \Delta t) e^{-j2\pi f_D \Delta t} d\Delta t. \tag{40}$$

–In the case of MB components,

$$S_h^{\text{MB}}(f_D, t) = \int_{-\infty}^{\infty} r_h^{\text{MB}}(t, \Delta t) e^{-j2\pi f_D \Delta t} d\Delta t. \tag{41}$$

IV. A 3D NON-STATIONARY WIDEBAND SIMULATION MODEL

Based on the proposed theoretical HST tunnel channel model described in Section III, the simulation channel model using the SoC [7] can be further developed. In the theoretical channel model, an infinite number of effective scatterers are assumed in each cluster, which can not be used for simulations in reality. Therefore, we need to approximate the distribution of scatterers with a discrete number of them.

A. Description of the Wideband MIMO Simulation Model

According to (2), the SoC simulation channel model for the link from p th Tx element to q th Rx element can be expressed as

$$\begin{aligned}
\tilde{h}_{pq}(t, \tau) &= \tilde{h}_{pq}^{\text{LoS}}(t) \cdot \delta(\tau - \tau^{\text{LoS}}(t)) \\
&\quad + \sum_{l=1}^L \tilde{h}_{pq,l}^{\text{SB}}(t) \cdot \delta(\tau - \tau_l^{\text{SB}}(t)) \\
&\quad + \sum_{i=1}^M \tilde{h}_{pq,i}^{\text{MB}}(t) \cdot \delta(\tau - \tau_i^{\text{MB}}(t)) \tag{42}
\end{aligned}$$

where

$$\tilde{h}_{pq}^{\text{LoS}}(t) = \sqrt{\frac{K_{pq}}{K_{pq} + 1}} e^{-j2\pi \frac{\varepsilon_{pq}(t)}{\lambda}} \times e^{j2\pi f_{R\max} t \cos(\tilde{\alpha}_R^{\text{LoS}}(t) - \gamma_R) \cos \tilde{\beta}_R^{\text{LoS}}(t)}. \quad (43)$$

The NLoS components consist of the SB and MB components totally. The SB components can be expressed as

$$\tilde{h}_{pq,l}^{\text{SB}}(t) = \sqrt{\frac{P_l}{(K_{pq} + 1)N_l}} \sum_{n_l=1}^{N_l} e^{j(\varphi_{n_l} - 2\pi \frac{\varepsilon_{pq,n_l}(t)}{\lambda})} \times e^{j2\pi f_{R\max} t \cos(\tilde{\alpha}_{\text{SR}}^{n_l}(t) - \gamma_R) \cos \tilde{\beta}_{\text{SR}}^{n_l}(t)}. \quad (44)$$

Moreover, the MB components of tunnel walls can be expressed as

$$\tilde{h}_{pq,i}^{\text{MB}}(t) = \sqrt{\frac{P_i}{(K_{pq} + 1)M_{i,1}M_{i,2}}} \times \sum_{m_{i,1}=1}^{M_{i,1}} \sum_{m_{i,2}=1}^{M_{i,2}} e^{j(\varphi_{m_i} - 2\pi \frac{\varepsilon_{pq,m_i,1,m_{i,2}}(t)}{\lambda})} \times e^{j2\pi f_{R\max} t \cos(\tilde{\alpha}_{\text{MR}}^{m_i,2}(t) - \gamma_R) \cos \tilde{\beta}_{\text{MR}}^{m_i,2}(t)}. \quad (45)$$

The simulation model is determined by discrete AoDs and AoAs that enable to better approximate the properties of the theoretical channel model, and the remaining parameters are identical to those of theoretical model. Hence, an accurate parameter computation method is essential to calculate these parameters. Algorithms to obtain the AoAs and AoAs, such as MEA, method of exact doppler spread (MEDS), and the L_p -norm method [7], are available. Here, we apply the MEA method to calculate the discrete angular values.

B. MEA for Parameterization of the Simulation Model

In this part, we take the SB cluster case as an example. The vectors of AAoAs and EAoAs were defined by $x = \{\alpha_{\text{SR}}^{n_l}, \beta_{\text{SR}}^{n_l}\}$. In the theoretical channel model, the cumulative distribution function (CDF) $F(x)$ of AAoAs and EAoAs with the term of $\int dF(x)$ [33] can be determined. In the simulation model, the MEA method is used to calculate N_l discrete vectors $x_{n_l} = \{\alpha_{\text{SR}}^{n_l}, \beta_{\text{SR}}^{n_l}\}_{n_l=1}^{N_l}$ according to $\int_{x_{n_l-1}}^{x_{n_l}} dF(a) = \frac{1}{N_l}$ to approximate the theoretical model. $F(x)$ can be divided into N_l sets with the same probability $1/N_l$. Therefore, in the vectors of AAoAs and EAoAs of the SB components, $x_{n_l} = \{\alpha_{\text{SR}}^{n_l}, \beta_{\text{SR}}^{n_l}\}$ can be obtained as $x_{n_l} = F^{-1}(\frac{n_l}{N_l})$, where F^{-1} is the inverse function of $F(\cdot)$. It should be mentioned that the AAoAs and EAoAs in the SB components and the MB components follow the von Mises distributions in the theoretical model. Hence, using this distribution, some discrete AAoAs and EAoAs can be obtained in the simulation model. Meanwhile, the AAoDs and EAoDs can also be obtained according to the geometrical relations between AAoAs and EAoAs in the SB components, and can be acquired by the mean values in the MB components.

C. Statistical Properties of the Simulation Model

1) *Time-Variant ST CF*: The time-variant ST CF can derived as

$$\begin{aligned} \tilde{R}_h(t, \Delta x_T, \Delta x_R, \Delta t) &= E \left[\tilde{h}_{pq}(t) \tilde{h}_{p'q'}^*(t - \Delta t) \right] \\ &= \tilde{R}_h^{\text{LoS}}(t, \Delta x_T, \Delta x_R, \Delta t) \\ &\quad + \tilde{R}_h^{\text{SB}}(t, \Delta x_T, \Delta x_R, \Delta t) \\ &\quad + \tilde{R}_h^{\text{MB}}(t, \Delta x_T, \Delta x_R, \Delta t) \end{aligned} \quad (46)$$

–In the case of LoS component,

$$\begin{aligned} \tilde{R}_h^{\text{LoS}}(t, \Delta x_T, \Delta x_R, \Delta t) &= \frac{1}{(K_{pq} + 1)} e^{j2\pi \frac{(\varepsilon_{p'q'}(t-\Delta t) - \varepsilon_{pq}(t))}{\lambda}} \\ &\quad \times e^{j2\pi f_{R\max} \Delta t \cos(\tilde{\alpha}_R^{\text{LoS}}(t-\Delta t) - \gamma_R) \cos \tilde{\beta}_R^{\text{LoS}}(t-\Delta t)}. \end{aligned} \quad (47)$$

–In the case of SB components,

$$\begin{aligned} \tilde{R}_h^{\text{SB}}(t, \Delta x_T, \Delta x_R, \Delta t) &= \frac{P_l}{(K_{pq} + 1)N_l} \sum_{n_l=1}^{N_l} \sum_{n_l=1}^{N_l} e^{j2\pi \frac{(\varepsilon_{pq,n_l}(t) - \varepsilon_{p'q',n_l}(t-\Delta t))}{\lambda}} \\ &\quad \times e^{j2\pi f_{R\max} \Delta t \cos(\tilde{\alpha}_{\text{SR}}^{n_l}(t) - \gamma_R) \cos \tilde{\beta}_{\text{SR}}^{n_l}(t)}. \end{aligned} \quad (48)$$

–In the case of MB components,

$$\begin{aligned} \tilde{R}_h^{\text{MB}}(t, \Delta x_T, \Delta x_R, \Delta t) &= \frac{P_i}{(K_{pq} + 1)M_{i,1}M_{i,2}} \sum_{m_{i,1}=1}^{M_{i,1}} \sum_{m_{i,1}=1}^{M_{i,1}} \sum_{m_{i,2}=1}^{M_{i,2}} \sum_{m_{i,2}=1}^{M_{i,2}} \\ &\quad \times e^{j2\pi \frac{(\varepsilon_{pq,m_{i,1},m_{i,2}}(t) - \varepsilon_{p'q',m_{i,1},m_{i,2}}(t-\Delta t))}{\lambda}} \\ &\quad \times e^{j2\pi f_{R\max} \Delta t \cos(\tilde{\alpha}_{\text{MR}}^{m_i,2}(t) - \gamma_R) \cos \tilde{\beta}_{\text{MR}}^{m_i,2}(t)}. \end{aligned} \quad (49)$$

Similar to the procedures applied in the theoretical channel model, the CCF and ACF for the simulation model can be derived by applying the discrete angular parameters. By setting Δt to 0 in (46), the spatial CCF of the 3D tunnel channel model can be expressed as

$$\tilde{\rho}_h(t, \Delta x_T, \Delta x_R) = E \left[\tilde{h}_{pq}(t) \tilde{h}_{pq}^*(t) \right] = \tilde{R}_h(t, \Delta x_T, \Delta x_R, 0). \quad (50)$$

By setting $\Delta x_R = 0$ and $\Delta x_T = 0$ in (46), the temporal ACF can be derived as

$$\tilde{r}_h(t, \Delta t) = E \left[\tilde{h}_{pq}(t) \tilde{h}_{pq}^*(t - \Delta t) \right] = \tilde{R}_h(t, 0, 0, \Delta t). \quad (51)$$

2) *Time-Variant Doppler PSD*: According to the PSD of the theoretical tunnel channel model in (38), the time-variant Doppler PSD of the simulation model $\tilde{S}_{h_{pq}h_{p'q'}}(f_D, t)$ can be obtained by the Fourier transform of (51) with respect to Δt , which can be illustrated as

$$\begin{aligned} \tilde{S}_h(f_D, t) &= \int_{-\infty}^{\infty} \tilde{r}_h(t, \Delta t) e^{-j2\pi f_D \Delta t} d\Delta t \\ &= \int_{-\infty}^{\infty} (\tilde{r}_h^{\text{LoS}}(t, \Delta t) + \tilde{r}_h^{\text{SB}}(t, \Delta t) + \tilde{r}_h^{\text{MB}}(t, \Delta t)) \\ &\quad \times e^{-j2\pi f_D \Delta t} d\Delta t. \end{aligned} \quad (52)$$

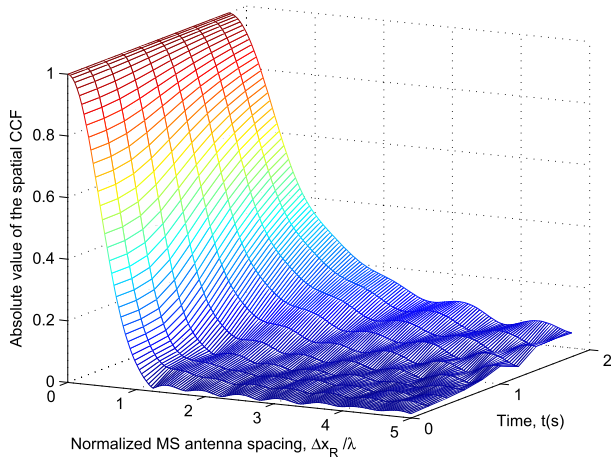


Fig. 5. Absolute values of the spatial CCFs of the 3D non-stationary tunnel channel model ($v_R = 360$ km/h, $k_1 = k_2 = 6$, $f_c = 2.4$ GHz).

V. RESULTS AND DISCUSSIONS

In this section, the statistical properties of the proposed tunnel channel models are investigated and analyzed. The parameters of the proposed cuboid model are listed or otherwise specified as in [34]. Here, we take a 2×2 MIMO linear antenna array communication system into consideration. With reference to Fig. 2, the locations of the Tx and Rx are defined by the Cartesian coordinates, which set Tx as $(x_T, y_T, z_T) = (0, 0.25, 4)$ and Rx as $(x_R, y_R, z_R) = (300, 3.2, 4)$, respectively. Also, basic parameters in this section are $f_c = 2.4$ GHz, $f_{R\max} = 800$ Hz, the length of tunnel $D = 300$ m, the antenna tilted angles of Tx and Rx are $\gamma_T = 0^\circ$, $\gamma_R = 0^\circ$, and the LoS Ricean factor $K_{pq} = K_{p'q'} = 14$. The z coordinate of tunnel top, z coordinate of tunnel bottom, y coordinate of tunnel left wall, and y coordinate of tunnel right wall are $z_t = 4.5$, $z_b = 0$, $y_{lw} = 0$, and $y_{rw} = 6.4$, respectively. In this paper, I_c clusters are assumed to be randomly placed on the internal surface of the tunnel, and each cluster includes several scatterers. In the following, the number of scatterers are $N_l = M_{i,1} = M_{i,2} = 50$.

A. Time-Variant Spatial CCF

Based on the proposed tunnel channel model, the non-stationarity of tunnel channel can be described effectively. By adopting antenna spacings $\Delta x_T = \lambda$, the absolute values of 3D spatial CCF of the proposed non-stationary tunnel channel model are illustrated in Fig. 5. From this figure, we can notice that the absolute values of spatial CCF change with time t because of the non-stationarity of the tunnel channel.

By using time-variant mean AAoA and EAoA in (20) and (21), Fig. 6 shows the comparison between the theoretical tunnel model and the simulation model for $\Delta x_T = \lambda$ at different time instants $t = 0$ s and $t = 2$ s. From this figure, we can notice that, even with time-variant AAoAs and EAoAs, the simulation model can provide a good approximation of the theoretical model at the same time. Due to the parameters of channel model change over the time, such as time-variant angular information, there is a difference between the spatial

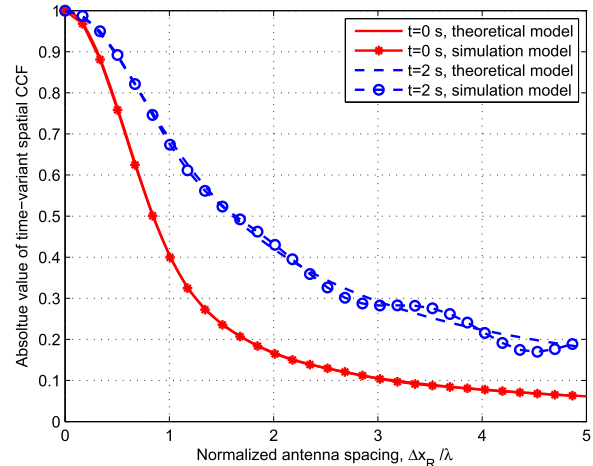


Fig. 6. Comparison between the spatial CCFs of the theoretical model and simulation model with time-variant angles at different time instants ($v_R = 360$ km/h, $k_1 = k_2 = 6$, $f_c = 2.4$ GHz).

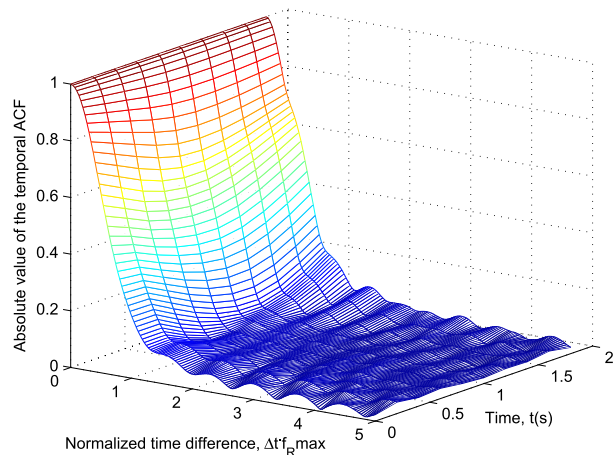


Fig. 7. Absolute values of the temporal ACFs of the 3D non-stationary simulation tunnel channel model ($v_R = 360$ km/h, $k_1 = k_2 = 6$, $f_c = 2.4$ GHz).

correlation properties with time-variant AoAs at different time instants.

B. Time-Variant ACF

Fig. 7 shows the absolute value of the 3D temporal ACF of the non-stationary simulation tunnel channel model for the NLoS case. Similar to the aforementioned spatial CCF, the absolute value of temporal ACF can vary with time t , due to the time-variant AoDs and AoAs.

Fig. 8 shows the absolute values of time-variant ACF of proposed theoretical model at different time instants. From this figure, we can observe a higher correlation when the LoS component is included compared to that obtained without it. Moreover, the non-stationary properties of the proposed channel model are demonstrated in this figure. At different time instants, i.e., $t = 0$ s and $t = 2$ s, there are different absolute values of time-variant ACF of the proposed channel model. On one hand, the non-stationarity of the proposed channel model can be reflected by using the time-variant angular information. On the other hand, time-variant angles will have an influence on the variation trend of ACFs.

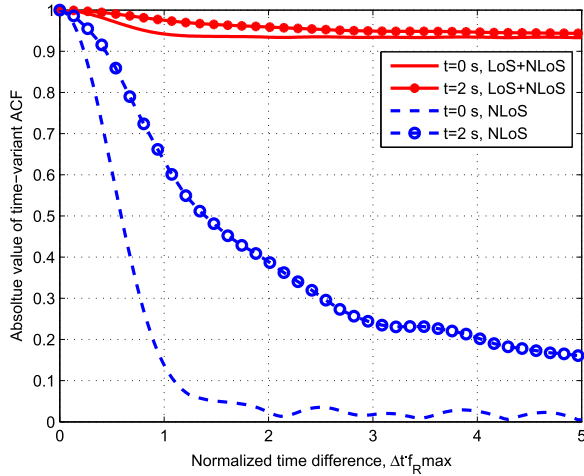


Fig. 8. Absolute values of the time-variant ACFs of the proposed simulation tunnel channel model with/without the LoS component at different time instants ($v_R = 360$ km/h, $k_1 = k_2 = 6$, $K_{pq} = 14$, $f_c = 2.4$ GHz).

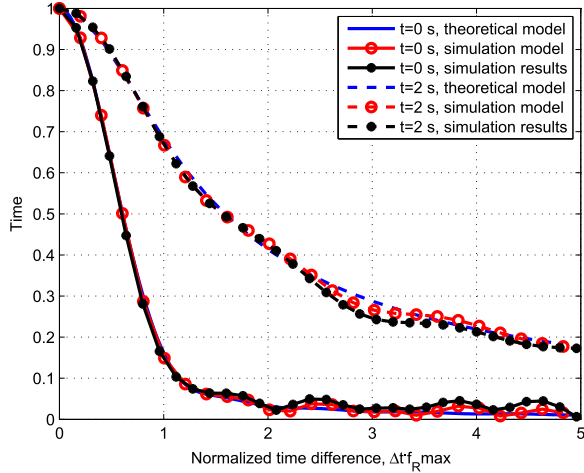


Fig. 9. Comparison among the time-variant ACFs of the theoretical model and simulation model and simulation results at the same time instant ($v_R = 360$ km/h, $k_1 = k_2 = 6$, $K_{pq} = 14$, $f_c = 2.4$ GHz).

Fig. 9 shows a comparison of the time-variant ACFs of the reference model, simulation model and simulation results at time instant $t = 0$ s. The simulation model provides a good approximation to the theoretical model in a small value of the time separation. Moreover, the simulation results match the simulation model to a good extent, which demonstrates a reasonable assumption when do the theoretical derivations and simulations.

C. Coherence Time

The coherence time is one of the important channel statistical properties, since it defines the time interval during which the channel can be seen as constant approximately. The CDF of the coherence time is shown in Fig. 10. From this figure, it can be deduced that there is a fairly short time duration in which the specific tunnel channel remains unchanged. The CDF of the coherence time of the simulation model, verified by the simulation results, can match that of the proposed theoretical GBSM. The coherence time can be calculated by $|r_c(t, \Delta t)| = \frac{1}{2} |r(t, 0)|$, which is defined as the smallest value of Δt to fulfil the above condition.

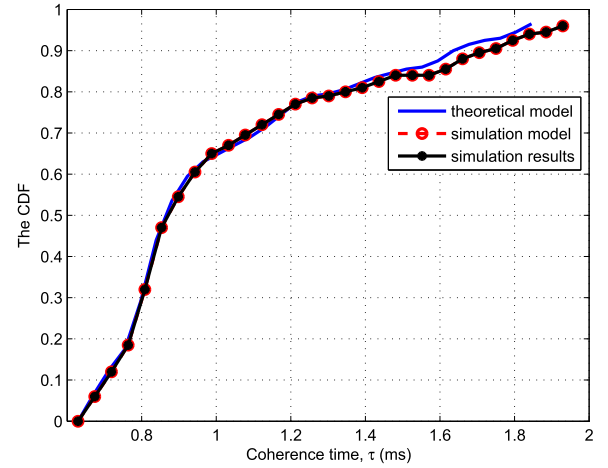


Fig. 10. The CDF of coherence time of the proposed tunnel channel models ($v_R = 360$ km/h, $k_1 = k_2 = 6$, $f_c = 2.4$ GHz).

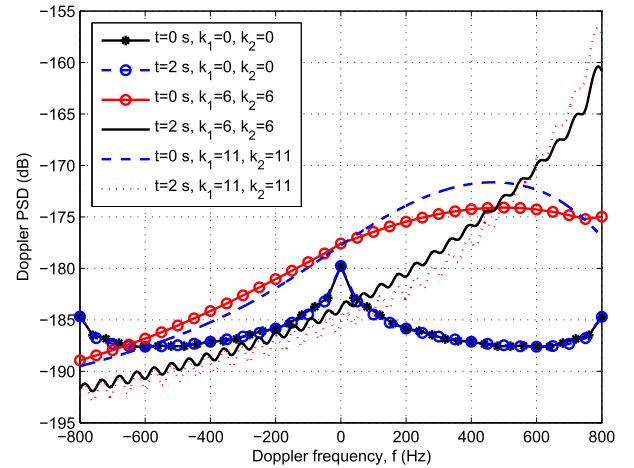


Fig. 11. Comparisons of time-variant Doppler PSDs of the simulation model for different k_1 and k_2 in different time instants ($v_R = 360$ km/h, $f_{Rmax} = 800$ Hz).

D. Time-Variant Doppler PSD

The PSD can be obtained by the normalised Fourier transform of the time-variant ACF, which is illustrated in Fig. 11. It shows the comparisons of time-variant PSDs of the theoretical model at different time instants and different k_1, k_2 values with $\Delta x_T = \Delta x_R = \lambda$. The PSDs at different time instants vary because of the non-stationarity of the proposed model, that is, the WSS condition on the time domain is unavailable due to the time-variant properties of the channel, and remain unchanged for isotropic case $k_1 = k_2 = 0$ at different time instants. We can easily notice that the Doppler PSDs are approximately symmetrical distributed along the Doppler frequency. Since the k_1, k_2 parameters control the width of the von Mises distribution and influence the values of AoAs, the angular parameters of the channel model will also affect the distribution of Doppler PSD. Different k_1, k_2 parameters will result in the variation trends of the PSDs to some extent. Moreover, it is noted that the smaller the coherence time of the channel, the larger the Doppler spread of the channel.

E. Time-Variant Correlation Matrix Distance (CMD)

To assess the similarity of channel statistics over angles and Doppler domains, some measures have been studied, such as

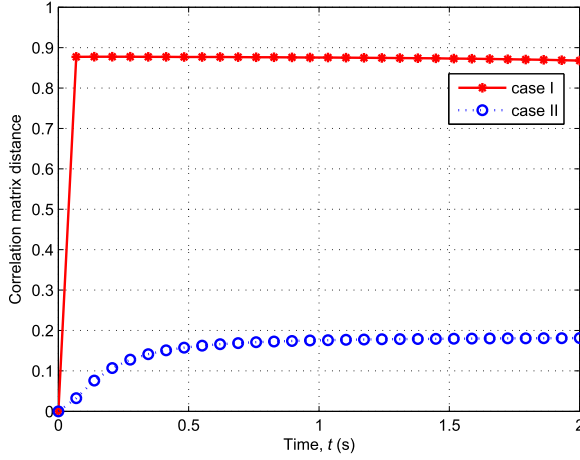


Fig. 12. Time-variant CMDs in case I and case II ($f_c = 2.4$ GHz, $v_R = 360$ km/h, $f_{Rmax} = 800$ Hz).

CMD [35] and local scattering function [36]. In the proposed model, the time-variant parameters, such as the AoDs and AoAs, are considered. To evaluate the non-stationary behavior of tunnel channel, the CMD metric is applied [35]. It can be calculated in space-time-frequency domain as follows:

$$d_{corr}(t_1, t_2; f_1, f_2; p, q) = 1 - \frac{\text{tr}\{R(t_1; f_1; p)R(t_2; f_2; q)\}}{\|R(t_1; f_1; p)\|_F \|R(t_2; f_2; q)\|_F} \in [0, 1] \quad (53)$$

where $\text{tr}\{\cdot\}$ is the trace operator, and $\|\cdot\|_F$ is the Frobenius norm. t_1, t_2 denote the different time constants, and f_1, f_2 denote the different frequencies. p and q are the p th antenna at Tx and q th antenna at Rx. $R(\cdot)$ denotes the correlation function. Here, we take the time domain as an example to study the changes of channel. The reference time is set as $t_1 = 0$, the CMDs at different times $d_{corr}(0, t_2)$, can be shown in Fig. 12. During the simulations, we selected two cases. Case I considers one cluster with SB components, and case II considers a twin-cluster with MB components. From Fig. 12, the changes of CMDs over time caused by the time-variant angles can be observed. Moreover, due to the different initial parameters, such as the distances of Tx-cluster and cluster-Rx, the CMDs in two cases change differently.

F. Comparison With Measurement Data

To verify the proposed HST tunnel channel models, we compare the stationary region of the measurement data obtained from [37] with that of our model using the following parameters: $f_c = 2.45$ GHz, $z_t = 5.3$, $z_b = 0$, $y_{lw} = 0$, $y_{rw} = 5.18$, and $D = 200$ m. The stationary region can be calculated by the following steps [7]:

- 1) The averaged power delay profiles (APDPs) can be calculated as

$$\bar{P}_h(t_k, \tau) = \frac{1}{N_{\text{PDP}}} \sum_k^{k+N_{\text{PDP}}-1} |\tilde{h}_{pq,i}(t_k, \tau)|^2 \quad (54)$$

where

$$\tilde{h}_{pq,i}(t_k, \tau) = \sum_{i=1}^I \tilde{h}_{pq,i}(t_k) \delta(\tau - \tau_i(t)). \quad (55)$$

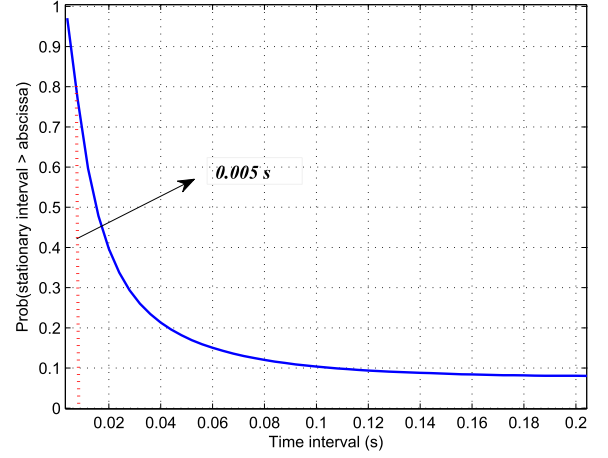


Fig. 13. Empirical CCDFs of stationary intervals for the proposed HST tunnel simulation model ($f_c = 2.45$ GHz, $v_R = 360$ km/h, $f_{Rmax} = 800$ Hz, $k_1 = 3$, and $k_2 = 3$).

Here, N_{PDP} denotes the number of power delay profiles to be averaged.

- 2) The correlation coefficient between two APDPs can be derived as

$$c(t_k, \Delta t) = \frac{\int \bar{P}_h(t_k, \tau) \bar{P}_h(t_k + \Delta t, \tau) d\tau}{\max\{\int \bar{P}_h(t_k, \tau)^2 d\tau, \int \bar{P}_h(t_k + \Delta t, \tau)^2 d\tau\}}. \quad (56)$$

- 3) The stationary interval can be expressed as

$$T_s(t_k) = \min\{\Delta t | c(t_k, \Delta t) < c_{\text{thresh}}\}. \quad (57)$$

Here, c_{thresh} is a pre-determined threshold of the correlation coefficient, which can be chosen as 80%.

- 4) The stationary region can be calculated as

$$d_{RS}(t_k) = \min\{\Delta x = v_R \cdot \Delta t | c(t_k, \Delta t) < c_{\text{thresh}}\}. \quad (58)$$

Based on the above steps, the empirical complementary CDFs of stationary intervals for our proposed HST tunnel simulation model are obtained as shown in Fig. 13, where the measurement data in [37] was selected as a reference. From this figure, we can notice that the stationary interval of the proposed HST tunnel channel is equal to 5 ms for 80% and 15 ms for 50%. In this case, the region of stationary is 0.5 m for 80% and approximately 1.5 m for 50%, which are in accordance with those in [37].

VI. CONCLUSIONS

In this paper, a 3D non-stationary theoretical GBSM for HST tunnel scenarios has been proposed by adopting MRS technology and DAS system. The MEA was used to obtain both the azimuth and elevation angles, and a corresponding simulation model has been developed. Numerical results have shown that the simulation model, verified by simulation results, can approximate closely the theoretical model in terms of key statistical properties. The time-variant statistical properties of the proposed theoretical and simulation models have also been investigated, which demonstrates that they can be used to describe non-stationary HST tunnel channels. It has also been shown that the time-variant angles will have

- [33] S. Wu, C. X. Wang, H. Haas, E. H. M. Aggoune, M. M. Alwakeel, and B. Ai, "A non-stationary wideband channel model for massive MIMO communication systems," *IEEE Trans. Wireless Commun.*, vol. 14, no. 3, pp. 1434–1446, Mar. 2015.
- [34] L. Gao, Z. Zhong, B. Ai, and L. Xiong, "Estimation of the Ricean factor in K the high speed railway scenarios," in *Proc. 5th Int. ICST Conf. Commun. Netw. China*, Beijing, China, Aug. 2010, pp. 1–5.
- [35] R. He *et al.*, "Characterization of quasi-stationarity regions for vehicle-to-vehicle radio channels," *IEEE Trans. Antenna Propag.*, vol. 63, no. 5, pp. 2237–2251, May 2015.
- [36] L. Bernadó, T. Zemen, F. Tufvesson, A. F. Molisch, and C. F. Mecklenbrucker, "The (in-) validity of the WSSUS assumption in vehicular radio channels," in *23rd Int. Symp. Pers., Indoor Mobile Radio Commun. (PIMRC)*, Sydney, NSW, Australia, Sep. 2012, pp. 1757–1762.
- [37] J. X. Li, Y. P. Zhao, J. Zhang, R. Jiang, C. Tao, and Z. H. Tan, "Radio channel measurements and analysis at 2.4/5 GHz in subway tunnels," *China Commun.*, vol. 12, no. 1, pp. 36–45, Jan. 2015.



Yu Liu received the B.Sc. and M.Eng. degrees in communication and information systems from Qufu Normal University, China, in 2010 and 2013, respectively, and the Ph.D. degree in communication and information systems from Shandong University, China, in 2017. Since 2017, she has been holding a post-doctoral position with the School of Information Science and Engineering, Shandong University. Her main research interests include non-stationary channel modeling, high-speed train wireless propagation characterization and modeling, and channel modeling for special scenarios.



Cheng-Xiang Wang (S'01–M'05–SM'08–F'17) received the B.Sc. and M.Eng. degrees in communication and information systems from Shandong University, China, in 1997 and 2000, respectively, and the Ph.D. degree in wireless communications from Aalborg University, Denmark, in 2004.

He was a Research Assistant with the Hamburg University of Technology, Hamburg, Germany, from 2000 to 2001, a Visiting Researcher with Siemens AG Mobile Phones, Munich, Germany, in 2004, and a Research Fellow with the University of Agder, Grimstad, Norway, from 2001 to 2005. He has been with Heriot-Watt University, Edinburgh, U.K., since 2005, where he was promoted to a Professor, in 2011. In 2018, he joined Southeast University, China, as a Professor. He has authored two books, one book chapter, and over 340 papers in refereed journals and conference proceedings. His current research interests include wireless channel modeling and (B)5G wireless communication networks, including green communications, cognitive radio networks, high mobility communication networks, massive MIMO, millimeter-wave communications, and visible light communications.

Dr. Wang is a fellow of the IET, an IEEE Communications Society Distinguished Lecturer in 2019 and 2020, and a Highly Cited Researcher recognized by Clarivate Analytics in 2017 and 2018. He received nine Best Paper Awards from the IEEE GLOBECOM 2010, IEEE ICCT 2011, ITST 2012, IEEE VTC 2013-Spring, IWCMC 2015, IWCMC 2016, IEEE/CIC ICC 2016, and WPMC 2016. He has served as a TPC member, the TPC chair, and the general chair for over 80 international conferences. He has served as an Editor for nine international journals, including the IEEE TRANSACTIONS ON WIRELESS COMMUNICATIONS from 2007 to 2009, the IEEE TRANSACTIONS ON VEHICULAR TECHNOLOGY from 2011 to 2017, and the IEEE TRANSACTIONS ON COMMUNICATIONS from 2015 to 2017. He was a Guest Editor of the IEEE JOURNAL ON SELECTED AREAS IN COMMUNICATIONS, Special Issue on Vehicular Communications and Networks (Lead Guest Editor), Special Issue on Spectrum and Energy Efficient Design of Wireless Communication Networks, and Special Issue on Airborne Communication Networks. He was also a Guest Editor of the IEEE TRANSACTIONS ON BIG DATA, Special Issue on Wireless Big Data.



Carlos F. Lopez received the B.Sc. and M.Sc. degrees in telecommunications engineering from the Universidad Politécnica de Madrid, Spain, in 2011 and 2015, respectively. He is currently pursuing the Ph.D. degree with the Institute of Sensors, Signals and Systems, Heriot-Watt University, Edinburgh, U.K. Since 2011, he has been working on the design and development of simulation tools for radio propagation prediction in mobile wireless communications systems. He is currently a Research Associate with the Institute of Sensors, Signals and Systems, Heriot-Watt University.

His research interests include mobile wireless communications, multiple-input multiple-output communication systems, and channel modeling.



George Goussetis (S'99–M'02–SM'12) received the Diploma degree in electrical and computer engineering from the National Technical University of Athens, Greece, in 1998, the B.Sc. degree in physics (Hons.) from University College London, U.K., in 2002, and the Ph.D. degree from the University of Westminster, London, U.K., in 2002.

In 1998, he joined Space Engineering, Rome, Italy, as an RF Engineer, and as a Research Assistant with the Wireless Communications Research Group, University of Westminster, U.K., in 1999. From 2002 to 2006, he was a Senior Research Fellow with Loughborough University, U.K. He was a Lecturer (Assistant Professor) with Heriot-Watt University, Edinburgh, U.K., from 2006 to 2009, and a Reader (Associate Professor) with Queen's University Belfast, U.K., from 2009 to 2013. In 2013, he joined Heriot-Watt, as a Reader, and was promoted to Professor, in 2014. He has authored or co-authored over 200 peer-reviewed papers five book chapters one book and two patents. His research interests include the modeling and design of microwave filters, frequency-selective surfaces and periodic structures, leaky wave antennas, microwave sensing and curing as well numerical techniques for electromagnetics.

Dr. Goussetis has held a research fellowship with the Onassis Foundation in 2001, a research fellowship with the U.K. Royal Academy of Engineering from 2006 to 2011, and a European Marie-Curie experienced researcher fellowship from 2011 to 2012. He was a co-recipient of the 2011 European Space Agency Young Engineer of the Year Prize, the 2011 EuCAP Best Student Paper Prize, the 2012 EuCAP Best Antenna Theory Paper Prize, and the 2016 Bell Labs Prize. He serves as an Associate Editor for the IEEE ANTENNAS AND WIRELESS PROPAGATION LETTERS.



Yang Yang (S'99–M'02–SM'10–F'18) is currently a Full Professor with the School of Information Science and Technology, ShanghaiTech University, China, serving as the Executive Dean of the School of Creativity and Art, and the Co-Director of the Shanghai Institute of Fog Computing Technology. Prior to that, he has held faculty positions with The Chinese University of Hong Kong, Brunel University, U.K., University College London, U.K., and SIMIT, Chinese Academy of Sciences, China.

He is a member of the Chief Technical Committee of the National Science and Technology Major Project New Generation Mobile Wireless Broadband Communication Networks from 2008 to 2020, which is funded by the Ministry of Industry and Information Technology of China. In addition, he is on the Chief Technical Committee for the National 863 Hi-Tech R&D Program 5G System R&D Major Projects, which is funded by the Ministry of Science and Technology of China. Since 2017, he has been serving the OpenFog Consortium as a Board Member and the Director of the Greater China Region. He is a General Co-Chair of the IEEE DSP 2018 Conference and a TPC Vice Chair of the IEEE ICC 2019 Conference.

He has published more than 200 papers and filed over 80 technical patents in wireless communications. His current research interests include wireless sensor networks, the Internet of Things, Fog computing, open 5G, and advanced wireless testbeds. He is a fellow of the IEEE.



George K. Karagiannidis (M'96–SM'03–F'14) was born in Pithagorion, Samos Island, Greece. He received the University Diploma (5 years) and the Ph.D. degree in electrical and computer engineering from the University of Patras, in 1987 and 1999, respectively. From 2000 to 2004, he was a Senior Researcher with the Institute for Space Applications and Remote Sensing, National Observatory of Athens, Greece. In 2004, he joined the faculty of Aristotle University of Thessaloniki, Greece, where he is currently a Professor with the Electrical and

Computer Engineering Department and the Director of the Digital Telecommunications Systems and Networks Laboratory. He is also a Honorary Professor at South West Jiaotong University, Chengdu, China.

His research interests are in the broad areas of digital communications systems and signal processing, with an emphasis on wireless communications, optical wireless communications, wireless power transfer and applications, molecular and nanoscale communications, and stochastic processes in biology and wireless security.

He has authored or co-authored more than 400 technical papers published in scientific journals and presented at international conferences. He has also authored the Greek edition of a book on telecommunications systems and has co-authored the book *Advanced Optical Wireless Communications Systems*, (Cambridge Publications, 2012).

Dr. Karagiannidis has been involved as the General Chair, the Technical Program Chair, and a member of the technical program committees of several IEEE and non-IEEE conferences. He was an Editor of the IEEE TRANSACTIONS ON COMMUNICATIONS, a Senior Editor of the IEEE COMMUNICATIONS LETTERS, an Editor of the *EURASIP Journal of Wireless Communications and Networks*, and several times Guest Editor of the IEEE JOURNAL ON SELECTED AREAS IN COMMUNICATIONS. From 2012 to 2015, he was the Editor-in-Chief of the IEEE COMMUNICATIONS LETTERS.

Dr. Karagiannidis is one of the highly-cited authors across all areas of electrical engineering, recognized from Clarivate Analytics as a Web-of-science Highly-Cited Researcher in the four consecutive years from 2015 to 2018.